Three-dimensional separation over unswept cantilevered wings at a moderate Reynolds number

Jacob M. Neal and Michael Amitay

Phys. Rev. Fluids **8**, 014703 — Published 19 January 2023

DOI: 10.1103/PhysRevFluids.8.014703

Three-dimensional separation over unswept cantilevered wings at a moderate Reynolds number

Jacob M. Neal and Michael Amitay*
Department of Mechanical, Aerospace, and Nuclear Engineering
Rensselaer Polytechnic Institute, Troy, NY 12180, USA
(Dated: January 5, 2023)

An experimental investigation of separated flows over unswept, cantilevered wings with a NACA 0015 cross-section is presented. For all experiments, the chord-based Reynolds number was 3.3×10^5. The results include qualitative surface topology from oil flow visualizations at angles of attack between 15° and 22° and semi-aspect ratios 1, 2, and 4, as well as quantitative three-dimensional flowfield measurements using Stereo Particle Image Velocimetry (SPIV) at an angle of attack of 22° and semi-aspect ratio 4. For all aspect ratios two counter-rotating surface foci appeared on the wings when reversed flow was present. At the lower aspect ratios, the surface foci did not occur until higher angles of attack due to a reduction in separation extent by downwash from the tip vortex which dominates a higher percentage of the span. The volumetric mean flowfield measured with SPIV over the semi-aspect ratio of 4 model and in its wake revealed the counter-rotating surface foci were connected by an arch vortex. Several vortex identification methods were employed to visualize the location of the arch vortex over the suction surface. The helicity and Reynolds stress fields were shown to be highly influenced by the shape of the arch vortex. The Reynolds shear stresses containing spanwise velocity fluctuations were influenced by the tip vortex and the root horseshoe vortex, and as such had greater magnitude than the spanwise Reynolds stresses measured in a previous study of an induced stall cell on a wall-to-wall wing. In addition, time-resolved flowfield measurements showed that power spectra at the stall cell center had a dominant shedding frequency of $St = 0.17$. At the center of the stall cell focus, the power spectra peaked at $St = 0.19$ and $St = 0.21$. Analysis of the instantaneous flowfield at the midspan characterized the shedding of vortices into the near-wake as an intermittent phenomenon where the magnitude of velocity fluctuations associated with the shedding would increase and decrease over time at periods on the order of ten shedding cycles.

I. INTRODUCTION

Flow separation has been studied for centuries, and remains a fluid mechanics problem that keeps researchers and design engineers busy to this day. To control separation on airfoils and wings is to ward off the parasitic effects of decreased lift and increased drag, which are coupled to this phenomenon. A detailed knowledge of the three-dimensional flowfield around such a stalled wing must be fully understood prior to launching an effective flow control strategy. To this end, the present study investigates the three-dimensional flowfield around unswept, cantilevered NACA 0015 wings with semi-aspect ratios $sAR = 1$, 2 and 4; at a range of angles of attack, $15° \leq \alpha \leq 22°$ and Reynolds number of $Re_c = 3.3 \times 10^5$. For the $sAR = 4$ and $\alpha = 22°$ case, a detailed study explained the mean flow topology on the wing's suction surface, the volumetric mean flow about the wing, and the unsteady shedding at select locations.

The three-dimensionality of the flow in the separated region around the mid-span of a stalled wing has interested many researchers. Winkelman and Barlow [1], and Boiko *et al.* [2] identified "mushroom-shaped" three-dimensional structures on the suction surface of stalled 2-D airfoils known as stall cells. These structures have two distinct counter-rotating surface normal vortices that have been referred to as the"owl eye" pattern. Stall cells have been known to form naturally on wings as long as critical wing shape, Reynolds number, aspect ratio, and angle of attack criteria are met. Stall cells are most often observed on unswept wings, though recent computations have visualized the stall cell pattern over swept back wings[3]. Yon and Katz [4] defined sub-regions of stalled angle of attack ranges, specifically shallow stall from $\alpha = 17°$ to $\alpha = 20°$ and deep stall at $\alpha > 20°$. They found that stall cells will occur in shallow stall but not in deep stall. Further, Broeren and Bragg [5] showed that the formation of the stall cell is characteristic of thick airfoils. McCullough and Gault [6] made the distinction that thicker airfoils stall more gradually as the separation builds up near the trailing edge and climbs towards the leading edge with increasing angle of attack. The formation of stall cells has only been observed to occur in this gradual stalling regime.

Weihs and Katz [7] recognized a spanwise periodicity of stall cells and defined a general relation for number of stall cells $n = AR/2.28$. Yon and Katz [4] provided a trend line from measurements on a NACA 0015 airfoil that had a number of cells $n = AR/2.3$, noting 2 stable stall cells for a model with $AR = 6$. Gross *et al.* [8] calculated the number of stall cells using lifting line theory and linked the number of the stall cells to the slope of the lift curve, where $n = -\frac{\pi}{4}\frac{\partial C_l}{\partial \alpha}$. Applying this to the lift and drag curves of Yon and Katz [4], they found good

* Correspondance: amitam@rpi.edu

agreement in the stall cell spacing where $n = AR/2.1$. Accordingly, the present results with $sAR \leq 4$ are expected to have at most a single cell.

Weihs and Katz [7] also linked the mechanism of stall cell formation to the Crow instability [9]. Specifically, they reasoned that the spanwise vortices which form at the leading and trailing edge of the stalled wing (i.e., the line vortices responsible for the von Karman street) develop spanwise undulations associated with the Crow instability wavelength and ultimately are pinched into spanwise cells of counter-rotating surface-normal vortices. Rodríguez and Theofilis [10] argued that the formation of stall cells is in fact due to a tri-global instability, arising from a stationary three-dimensional eigenmode in the steady flowfield. This stationary nature of the eigenmode is reflected in the ability of experimentalists to visualize the owl eye pattern on the surface with oil. He *et al.* [11] expanded this result to show, using modal and non-modal linear stability analysis, that two modes with short and long spanwise wavelength are responsible for the destabilization of the separated flowfield.

The unsteadiness associated with airfoil stall has been documented for many years, driven by the detrimental tendency for stalled wings to experience periodic fluctuations in aerodynamic loads, which plagues the fatigue life of the wing as well as the aircraft to which it is attached. Fluctuations in the stall cell shear layers were evaluated by Dell'Orso *et al.* [12] with volumetric SPIV measurements of the stall cell flowfield, finding that the Reynolds stresses were highest within the recirculation region inside the cell. Two ranges of frequencies tend to be seen in power spectral density estimates measured inside the stall cell. Zaman [13] noted that a 2D wing at a high angle of attack would exhibit a spectral peak associated with bluff-body-type shedding at $St = 0.2$, but also saw the presence of a frequency one order of magnitude lower. Similar frequencies have since been reported in the DNS results of Liu et al. [14], who also noted the presence of frequencies an order of magnitude higher than the shedding frequency corresponding to the Kelvin-Helmholtz shear layer mode. Critical point theory [15] of describing complex flowfields in terms of nodes or saddle points has been used to characterize 3D separation in both mean flow and instantaneous measurements [2][16]. Maltby's [17] oil flow visualization method is especially useful to elucidate mean skin friction lines near the suction surface and has historically been the primary way to identify stall cells. More recently, Ma *et al.* [18] measured planes of time-resolved PIV near the suction surface and tracked critical points' path over time, deducing that the stall cell shape can be the result of a time average of the advection of both forward and backwards stall cell shaped stagnation lines.

Manolesos *et al.* [19] showed that the onset and location of stall cells can be controlled using passive disturbances. Spanwise zig-zag tape placed near the leading edge of a 18% thickness cambered wing induced and more notably *fixed the location* of the stall cells that formed on the suction side. Numerical results of the same configuration showed the same spatial stabilization of the stall cell as the experiments. SPIV and oil flow visualizations by Demauro et al. [20] identified the ranges of angles of attack and Reynolds numbers that lead to stall cell formation over a quasi-2D NACA 0015 wing in shallow stall. Investigating the same experimental model, Dell Orso et al. [12] highlighted the effect of partial and full span trips using zig-zag tape showing that the disturbance leads to the formation of stall cells at lower Reynolds numbers than the case without the presence of the zig-zag tape.

The present work aims to combine the scopes of previous works by analyzing the volumetric mean flow and the unsteady shedding of unswept, cantilevered, low aspect ratio wings. The signature of the vortical structures on the wing's surface is addressed using oil flow visualization (OFV), the volumetric mean flow is reconstructed by stacking planes of stereoscopic particle image velocimetry (SPIV) data, and the unsteady shedding is measured using time-resolved SPIV (TR-SPIV). The effects of aspect ratio of these cantilevered wings are explored and discussed.

II. EXPERIMENTAL SETUP AND PROCEDURE

The experiments were conducted at Rensselaer Polytechnic Institute's Center for Flow Physics and Control (CeFPaC). The open-return wind tunnel used has a test section that is 5 m long with a 0.8 m x 0.8 m cross section and a maximum speed of 50 m/s. Upstream of the test section, flow passes through a flow conditioning unit that is composed of a perforated plate, honeycomb and screens, resulting in a freestream turbulence intensity of less than 0.2%. Experiments were performed on a NACA 0015 airfoil with a chord length $c = 0.127$ m and a modular semi-span that could achieve semi-aspect ratios of $sAR = 1$, 2 and 4. Figure 1 shows the experimental model, which was mounted at mid height within the wind tunnel test section to minimize tunnel wall effects. Additionally, a fence starts a fresh wall boundary layer a few chord-lengths upstream of the mounted model. As detailed in the figure, the angle of attack was set facing up for oil flow visualization and facing down for the particle image velocimetry data collection.

A. Oil Flow Visualization Setup

Oil flow visualization experiments were used to identify and characterize the signature of different flow structures on the model's suction surface. These experiments were conducted at angles of attack between $\alpha = 15°$ and $\alpha = 22°$ and at chord-based Reynolds number of $Re_c = 3.3 \times 10^5$ for aspect ratios of $sAR = 1$, 2 and 4. A thin film of engine oil (SAE0W20) was applied to the model's suction side using a paintbrush. A sparse,

thin layer of fluorescent powder (T13 "Rocket Red" Pigment by DayGlo) was sprinkled onto the oil. The powder was illuminated using two three-channel DMX-512 light-emitting diode (LED) ultraviolet arrays. Images were captured with a Canon EOS 77D camera with a 550 nm long-pass filter. The orientation of the model, camera, and lighting are shown in figure 1a. The wind tunnel was ramped up to the free stream velocity, and images were collected in bursts of 3 using an auto-exposure bracketing (AEB) method. Each image in the bracket had a different exposure time, defined by a bias value from a baseline exposure time. The camera then optimized the F-stop and the ISO speed for each image in the bracket. The variance of these parameters used in the present results are listed in Table I. The three images in the bracket were merged into a single high dynamic range image during post-processing with Photomatix software.

The vortical structures in the mean flow over the model pulled the oil along their trajectory (to regions of low shear), and the fully developed signature was illuminated by the fluorescent pigment. The flow was considered to reach steady state if the patterns in the oil and pigment remained stationary for 10 minutes.

This OFV method was conducted on several NACA 0015 models. The first configuration was a cantilevered model of $sAR = 4$. A similar model had been tested previously by Dell'Orso et al. [21] in a wall-to-wall configuration. In their study, a map of the different types of separation patterns that can occur over a range of Reynolds numbers and angles of attack was generated. Since the present research was performed on cantilevered wing models, it was necessary to determine if a similar stall pattern map could be repeated. Following the OFV on the $sAR = 4$ model, this method was performed on two more cantilevered models of semi-aspect ratios $sAR = 2$ and 1.

B. Stereo Particle Image Velocimetry Setup

One case, examined using OFV, was further explored using Stereoscopic Particle Image Velocimetry (SPIV). Specifically, the mean flowfield around the cantilevered model with semi-aspect ratio $sAR = 4$ at an angle of attack $\alpha = 22°$ and Reynolds number $Re_c = 3.3{\times}10^5$ was measured. SPIV images were acquired using two Lavision Imager LX 2 Megapixel cameras. Each camera had a 35 mm lens and a 532 +/- 10 nm notch filter to only allow the green laser light to pass through. The laser used was the New Wave Solo PIV 120 $mJ/pulse$ per pulse Nd-Yag (532 nm). Since the angle of attack of the model was kept fixed at $\alpha = 22°$, the cameras were mounted on a bracket that was at the same angle, to maintain a stereoscopic view that was parallel to the airfoil chord. Scheimpflug adapters were used to focus each camera onto the laser sheet plane. The wall at the root of the wing model was covered in black light-absorbing paper to minimize laser reflections. This setup is shown in figure 1b.

In order to measure a volumetric flowfield, a series of streamwise (x-y) planes was collected at multiple spanwise locations. Each data plane contained the streamwise, vertical, and spanwise velocity distributions (U, V, and W respectively). The laser and the cameras were mounted on separate computer-controlled traverses, both parallel to the free stream, and for every spanwise location the laser and cameras traverse would translate the same distance along the span. Planes were collected at 6 mm ($z/b = 0.01$, where b is the length of the wing span) spanwise increments. At every spanwise plane, self-calibration was performed to account for any slight misalignment of the laser sheet that may have occurred during the spanwise translation of the PIV equipment. To focus on the large scale counter-rotating structures at the midspan, planes were collected along the range $0.45 < z/c < 3.75$ where c is the chord length, or $0.1125 < z/b < 0.9375$. Data acquisition was performed by the DaVis software, where 500 images pairs were collected at each plane, using interrogation windows of 64 × 64 pixels for the first pass and 32 × 32 pixels for the second and third passes with 50% overlap. The time increment for each image pair was 35 μs. The time-averaged data ($\overline{U}$, $\overline{V}$, and $\overline{W}$), and the Reynolds stresses ($\overline{u'u'}$, $\overline{v'v'}$, and $\overline{w'w'}$) of these planes were then stitched together to obtain the flow volume.

TABLE I: Auto-exposure bracketing settings used on the DSLR camera in the oil flow visualization experiment. Exposure baseline was 1.3 seconds.

F-stop	ISO speed	Exposure bias
f/4	ISO-400	+0.3
f/4	ISO-200	-1
f/4.5	ISO-100	-1.3

C. Time-resolved Stereoscopic Particle Image Velocimetry Setup

Two spanwise locations along the $sAR = 4$ model were selected for further investigation using time-resolved SPIV (TR-SPIV). The orientation of the model, laser sheet, and cameras was identical to the SPIV setup shown in figure 1b. However, for the TR-SPIV, two 4 Megapixel CMOS cameras were used with 100 mm lenses. The laser used was a ND:YLF dual head unit capable of 30 mJ/pulse of 527 nm wavelength light. The time increment for each image pair was set to 11 μs, and the sampling frequency was varied depending on the size of the interrogation window. At each spanwise location, data at streamwise (x-y) planes were collected in the near wake. Due to constraints in the TR-SPIV hardware, the area of the PIV plane scales inversely with the max sampling frequency. Therefore, the planes measured in the wake with area $70mm \times 120mm$ were sampled at highest at-

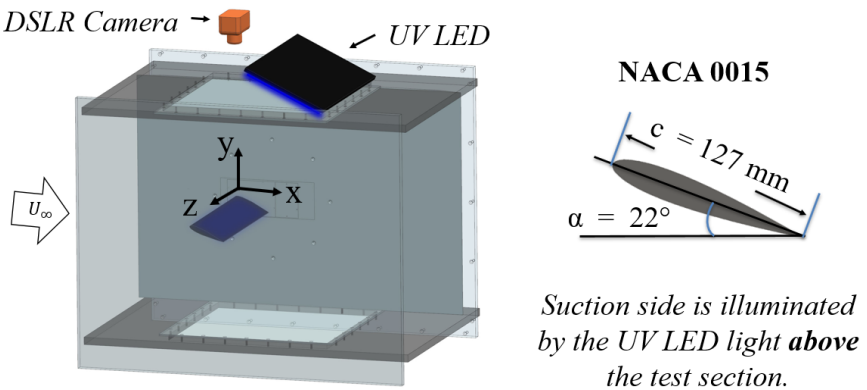

(a)

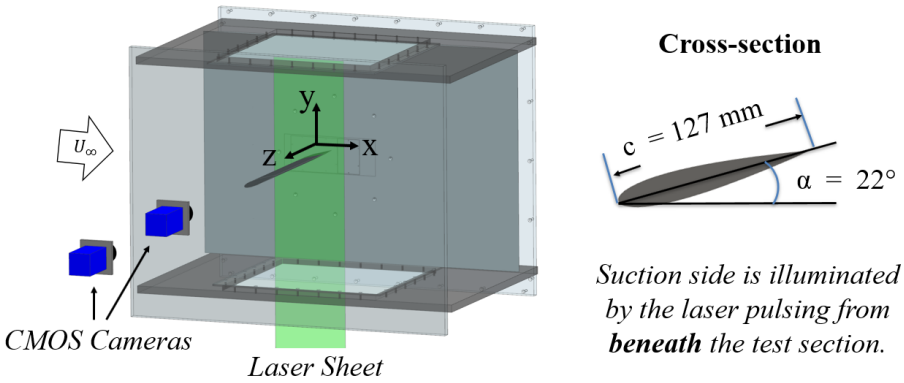

(b)

FIG. 1: Experimental setups for (a) oil flow visualization, and (b) particle image velocimetry.

tainable rate of $F_s = 2074Hz$, and 7,708 image pairs were collected, giving a frequency resolution of 0.269 Hz.

D. PIV Uncertainty

The quality of the SPIV and TR-SPIV data was verified with an uncertainty analysis. Sciacchitano [22] recommends the value of uncertainty of time-averaged PIV planes to be calculated using the method of Benedict and Gould [23] for calculating uncertainty of turbulence statistics. The uncertainty of the time-averaged streamwise component $U_{\overline{U}}$ is shown in equation 1 as a ratio of the standard deviation of the velocity component, σ, to the number of images collected, N.

$$U_{\overline{U}} = \frac{\sigma_{\overline{U}}}{\sqrt{N}} \tag{1}$$

The magnitude of uncertainty of each mean velocity component is directly linked to the unsteadiness in the flow, so it is expected that the highest uncertainty will be near shear layers, mixing layers, and unsteady wakes. The uncertainty for the time-averaged planes of streamwise velocity for both SPIV and TR-SPIV measurements were calculated, and since the TR-SPIV was only performed at two spanwise locations, these same locations are compared to the same planes from the SPIV volume. The uncertainty for time-averaged streamwise velocity remains below 2.5% throughout the measurement domain. The uncertainty of the time-averaged streamwise velocity for the TR-SPIV remains below 0.1% of the freestream velocity. This large difference in uncertainty is due to the large difference in the number of images collected for the SPIV cases and the TR-SPIV cases.

Following the derivations in Sciacchitano [22], a good estimate for the uncertainty in the Reynolds stress and TKE fields are represented in Equations 2-4. The uncertainty of each Reynolds stress, $U_{\overline{u_i^2 u_i^2}}$, can be expressed as follows:

$$U_{\overline{u_i' u_i'}} = \overline{u_i' u_i'} \sqrt{\frac{2}{N}} \tag{2}$$

The turbulent kinetic energy is defined as half of the

sum of the Reynolds stresses, and based on the error propagation formula, the uncertainty in TKE is defined as follows:

$$U_{TKE} = \frac{1}{2}\sqrt{(U_{\overline{u'u'}})^2 + (U_{\overline{v'v'}})^2 + (U_{\overline{w'w'}})^2} \quad (3)$$

Assuming that $N >> 1$ and the instantaneous measurement uncertainty is negligible with respect to the magnitude of velocity fluctuations, the result of Equation 3 can be used and the expression for U_{TKE} is reduced to:

$$U_{TKE} = \sqrt{\frac{1}{2N}}\sqrt{(\overline{u'u'})^2 + (\overline{v'v'})^2 + (\overline{w'w'})^2} \quad (4)$$

Based on these derivations, the uncertainty of TKE is less than 1.25%.

Contribution to bias errors may occur from camera focus, incorrect choice of time increment between image pairs, or (especially pertinent to the volumetric data acquisition method) misalignment of the traverses which are assumed to move in parallel from one spanwise location to the other. The alignment of the traverse was verified by a simple experiment of checking the camera focus on the laser sheet at the inboard and outboard limits of the data collection volume. As long as the camera remains in focus along the span as traversed by coupled translations of the camera and the laser, the traverses must be parallel. The focus quality within each individual plane is assumed to be within the depth of field of the 35 mm lenses, which is ± 0.5 mm. In addition, the use of Scheimpflug adapters and stereo-self calibration are seen to minimize any planar focus or particle shift issues.

III. RESULTS

This section discusses the results of the wind tunnel experiments to explore the flow structures on a finite span, cantilevered, low aspect ratio wing at high angles of attack. Three sets of experiments were conducted: qualitative parametric study using surface oil flow visualizations, mean volumetric flowfield mapping over the model and in its near wake using SPIV, and more detailed examination of the near wake at two spanwise locations using planar TR-SPIV.

A. Oil Flow Visualization Results

The first set of experiments were the OFV, where three semi-aspect ratio ($sAR = 1$, 2 and 4), cantilevered unswept wings were tested at a Reynolds number of $Re_c = 3.3 \times 10^5$, and angles of attack of $\alpha = 15°$ to 22°. Figure 2 displays these results. For each of the aspect ratios studied, increasing angle of attack leads to the inevitable separation accompanied by two counter-rotating surface foci. In the figure, the top (inboard) focus for each wing rotates clockwise and the bottom (outboard) focus rotates counter-clockwise. As aspect ratio is decreased, these surface foci are closer together and interact differently.

Yen and Huang [24] reported oil flow visualizations for an unswept finite wing with $sAR = 5$ and NACA0012 cross section. They noted at $\alpha = 9°$ the flow exhibits a leading edge separation bubble which transformed to a turbulent separation pattern and then 3D separation at $\alpha = 11°$ and 15°, respectively. These patterns were observed to be relatively independent of Reynolds number for the range of $Re_c = 0.46 \times 10^5$ to 1.2×10^5. The 3D separation patterns in the present results (all $\alpha > 15°$) are similar to the patterns of turbulent separation with counter-rotating foci, and the present results expand the angle of attack range between the discrete values chosen by [24].

Figure 2 presents the OFV results for these three semi aspect ratios at angles of attack $\alpha = 15°$ to 22°, giving a qualitative sense of the signatures of flow features on the models' suction surface. The cases exhibiting reverse flow are emblazoned with a blue arrow in the reversed flow direction. Counter-rotating surface foci were present as long as reversed flow exists on the suction surface for each aspect ratio. For lower aspect ratios, the foci and reversed flow appeared at higher angles of attack. For $sAR = 4$ the foci were present for all angles of attack tested, but for $sAR = 2$ the foci were present only for $\alpha \geq 17°$ and for $sAR = 1$ they were present only for $\alpha \geq 20°$. These counter-rotating outboard and inboard surface foci occur near the wing tip and the wall, respectively, showing that they are directly related to the end effects of the wing. More accurately, they are the result of interaction between the reversed flow at the midspan and the attached flow near the wing tip and the wall. Without these end effects, one would expect to see reversed flow across the entire wing span.

The tip vortex interaction is the cause of the outboard focus at each aspect ratio. The tip region is highly influenced by the tip vortex, as seen with the high shear stresses pulling oil off the corner of the tip and the trailing edge. This tip vortex effect is labeled 'TV effect' in figure 2 at $sAR = 4$, $\alpha = 15°$, 18°, and 21° occurs across a roughly triangular shape near the tip (marked in the figure with white dotted lines) that decreases in size with increase in α. For moderate to low aspect ratio finite wings, the tip vortex has been shown to reattach flow near the wing tip at high angles of attack [25][26]. As such, the tip vortex serves to reattach the flow near the wing tip, and this reattached flow interacts with the separated flow at the midspan to create the outboard counter-clockwise rotating surface focus point. For lower aspect ratio wings, this effect of the tip vortex is stronger, and delays the angle of attack where reversed flow is present over the wing.

For the $sAR = 4$ case, the pattern exhibited in figure 2 of the midspan reversed flow being surrounded by two counter-rotating surface foci is similar to the flow vi-

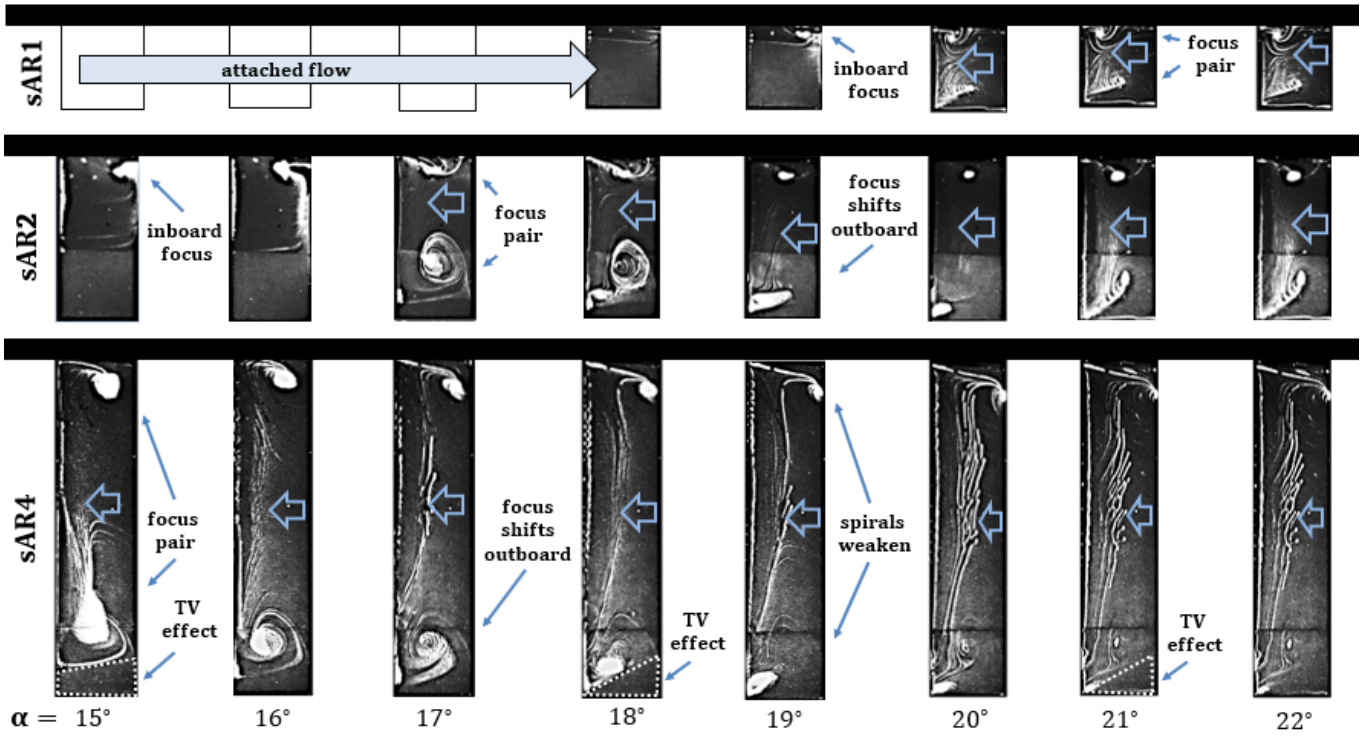

FIG. 2: OFV on the wings' suction surface, where $sAR = 1$ (upper row), 2 (mid row), and 4 (bottom row), with increasing angle of attack from left to right for Reynolds number $Re_c = 3 \times 10^5$. Flow is from left to right, where the root and tip of the models are on the upper and lower sides, respectively, of each image.

sualizations seen at similar angle of attack for a higher aspect ratio finite wing by Winkelmann [27]. Each focus is created by interaction of the midspan separation with either the tip vortex or the root vortex. Near the corner of the leading edge and the root, the inboard focus formed by an interaction between the horseshoe vortex at the root and the midspan separation. The boundary layer along the wall and the root vortex combine to have a reattachment effect similar to that of the tip vortex. For the model with $sAR = 2$, the reversed flow region was only prevalent over the inboard half of the span. On either side of the reversed flow region were two counter-rotating structures; however, unlike the $sAR = 4$ case, these foci were not symmetric across the span. In fact, the inboard focus was farther upstream than the outboard focus. The $sAR = 1$ model also exhibited reverse flow and counter-rotating foci. However, for this case, the outboard focus merged with the high shear stress region near the tip, while the inboard focus was near the leading edge and root corner, and merged with the horseshoe vortex. These results are similar to the low aspect ratio flow visualizations of Neiland and Stolyarov [28], most notably in the skew in streamwise location of the respective surface foci.

Note that for $sAR = 4$, the counter-rotating surface foci were concentrated spirals at lower angles of attack, but with increasing α the foci left weaker and weaker imprints in the oil. It appears that the surface foci get weaker as the wing gets deeper into stall. Since the surface foci are caused by interactions between the end conditions (tip vortex and horseshoe vortex) and the midspan conditions (flow separation and reversed flow) this interaction will get weaker as any of these contributing factors gets weaker. Of course, as angle of attack increases beyond the stall angle, the adverse pressure gradient will increase as will the extent and severity of the separation. As less lift is produced by the wing at post-stall angles of attack, the circulation of the tip vortex will decrease. There is evidence of this in the OFV, for example, the $sAR = 4$ case at $\alpha = 15°$e in figure 2. The outboard surface spiral is close to the midspan, and with increasing α this spiral moved outboard. As a result, the effect of the tip vortex reduces to a small region near the tip. This could be because the tip vortex is weakening, the midspan separation is intensifying, or both. It is expected that the separation intensity to increase with higher α, and the tip vortex to decrease in circulation as less lift is produced during stall, which is linked to a decrease in the bound circulation on the wing. This weakens the interaction between the tip vortex and the separation region; thus, weakens the surface foci.

The OFV results show that for semi-aspect ratios $sAR = 1$, 2, and 4, the outboard and inboard surface foci are formed due to interactions of the midspan sepa-

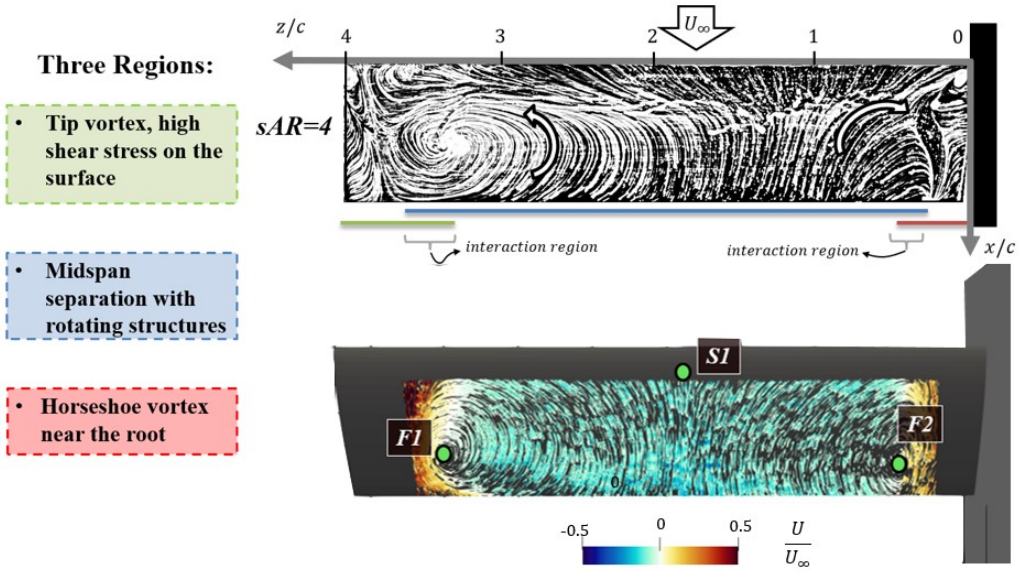

FIG. 3: OFV on the wing's suction surface (top), and SPIV streamlines colored by streamwise velocity (bottom), where $sAR = 4$, detailing the three characteristic regions that are seen over cantilevered wings.

ration with the tip vortex and horseshoe vortex, respectively. Since these foci stay the same normalized distance away from the wing tip and root for each aspect ratio, they must be the direct result of the end effects. Consequently, at lower aspect ratios the tip vortex interactions and root vortex interactions are closer together and both serve to suppress separation until a higher angle of attack than for the large aspect ratio case.

B. Time-Averaged Flowfields

To explore the vortical structures that were present over the $sAR = 4$ model, as identified by their signature on the surface using the OFV, SPIV measurements of the entire flowfield above the suction surface and into the near wake were acquired. Figure 3 compares the near surface streamlines calculated with the SPIV flowfield to the flow visualizations, showing excellent agreement in the location of the surface foci and the reversed flow region. Near the surface, the presence of the reverse flow region across most of the span was clearly visible. On either side of the reversed flow region, two counter-rotating foci were seen, labeled in the figure as F1 and F2. Included in figure 3 is the tentative location of the saddle point S1 at the stagnation point of the cellular separation. The actual location of this saddle point lay outside the measurement domain, but would be expected to reside at the spanwise location with least spanwise flow, which is identified through the trajectories of the 3D streamlines.

Since the surface measurements compare well with the OFV, the time averaged flowfield over the model is presented next. First, the time-averaged three-dimensional streamlines, colored by streamwise velocity normalized by the freestream $\overline{U}/U_\infty$, are presented in figure 4a. The reverse flow region across most of the span was characterized by a coiled up spiral that extends into the wake, indicative of a large separation bubble. To further explore the flowfield over the model and in its wake, four streamwise (x-y) planes of spanwise vorticity normalized by the freestream and the chord length $\omega_z c/U_\infty$, superimposed with in-plane streamlines, are shown in figure 4b. Note that these streamlines all wrap into a clear focus point within the contours of negative vorticity. The location of this focus point, as well as the corresponding focus point in other x-y planes (not shown) was tracked along the span, and visualized with the green spline shown in figures 4a and b. This three-dimensional focus originates and terminates on the suction surface at locations similar to the qualitative OFV results reported in the previous section. It should be noted that a *vortex* is not identified with this representation. According to Jeong [31], the lack of Galilean invariance in streamlines does not make them an adequate vortex identification criterion. That being said, the streamlines still give a clear characterization of the trajectories of the mean flow, especially when showing an entire volume.

The location of the separation vortex was investigated using a couple of vortex identification methods. First, Γ_1 criterion was calculated following the planar method from Graftieaux *et al.* [32]. To take into account out-of-plane rotation, the Γ_1 was calculated in 3D, resulting in a three-component vector of Γ_1 magnitudes in x, y, and z. Figure 4c shows the contour of the highest magnitude level of the Γ_1 vector in red, superimposed with the separation bubble (contour of $\overline{U} = 0$) in yellow. Another vortex identification method is presented in figure

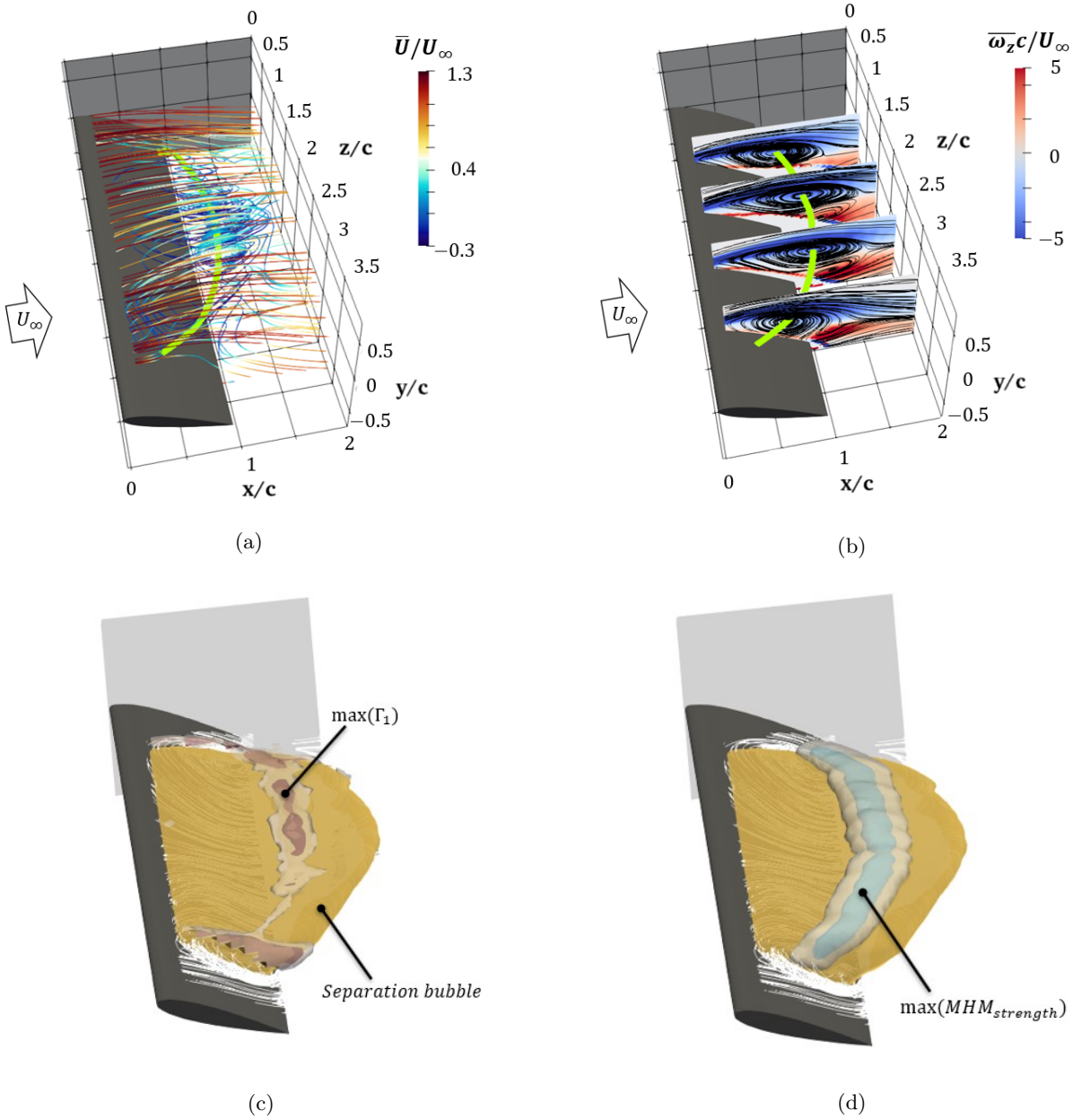

FIG. 4: Time-averaged flow volume for $sAR = 4$ wing with (a) three-dimensional streamlines colored with normalized streamwise velocity, (b) streamwise planes of normalized spanwise vorticity superimposed with in-plane streamlines, where the green line tracks the location of separation vortex core, (c) contour of the highest magnitude level of the Γ_1 vector (red), superimposed with the separation bubble ($\overline{U} = 0$) in yellow, and (d) contours of the Modified Holmen Method (MHM) Carvajal *et al.* [29] based on the method from Holmén [30].

4d. The Modified Holmen Method (MHM) was developed by Carvajal *et al.* [29] based on the method from Holmén [30]. Note that the streamline-tracing and MHM methods are entirely planar, that is, they do not take into account spanwise velocity gradients. The Γ_1 and the 3D streamlines are volumetric methods that take into account rotation in all three directions. All methods agree well on the spatial location of the separation arch vortex.

The effect of the arch vortex on the upwash and downwash of the mean flow was examined using the vertical flow component, hereafter referred to as $vflow$. The $vflow$ is related to the concept of the backflow parameter: a scalar flowfield quantity used by Simpson [33] to characterize the percentage of the time that flow is reversed. When backflow parameter is equal to one half, then half the time the flow is forward and half the time it is backwards, hence marking the location where the average streamwise velocity is zero, or, as the present

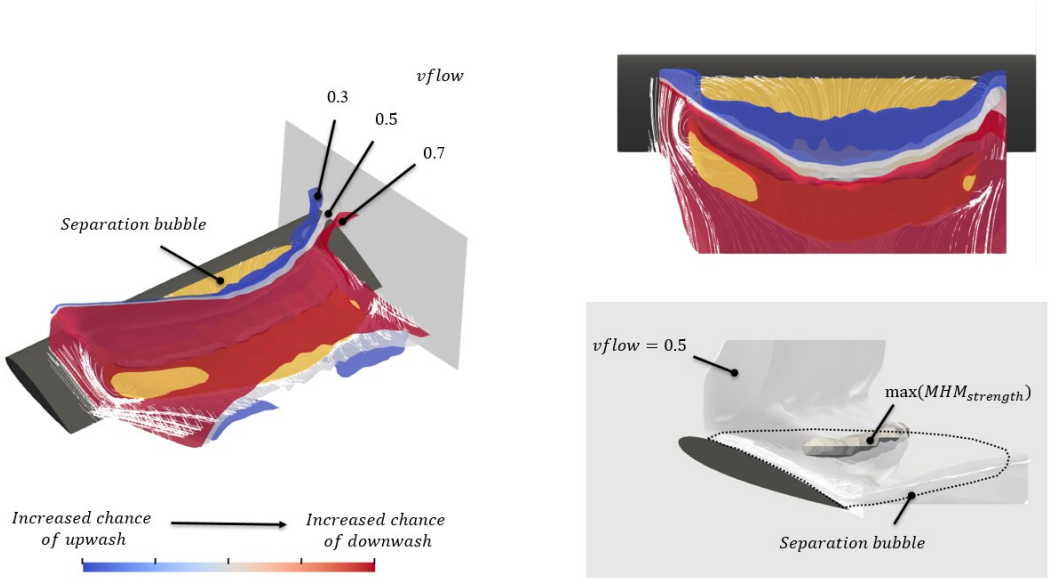

FIG. 5: Color contours of the vertical flow parameter, superimposed with a contour of the separation bubble (contour of $\overline{U} = 0$), and the separation vortex core visualized with MHM strength.

analysis characterizes the separation bubble: $\overline{U} = 0$. To characterize the likelihood of upwash and downwash, the $vflow$ measures the percentage of time that the *vertical* component of velocity is positive or negative. Three levels of $vflow$ (0.3, 0.5, 0.7) are shown in figure 5. The contour of $vflow = 0.5$ (white) exactly tracks the 3D location of the arch vortex. The separation vortex, tracked with maximum strength of the MHM, is aligned with the curved lobe in the $vflow = 0.5$ contour. This contour also has a separate concentration tracing the path of the trailing edge vortex as it rises in the wake to the downstream terminus of the separation bubble.

The distribution of the spanwise component of velocity over the model and in its wake was also investigated and is presented in figure 6. Figure 6a presents spanwise (y-z) planes of color contours of normalized spanwise velocity, superimposed with in-plane streamlines. The OFV and SPIV have both clearly indicated that the flowfield is highly three-dimensional. In fact, the only region in the flowfield that could be considered somewhat two dimensional is the streamwise (x-y) plane at the spanwise location of $S1$. The planes in figure 6a show that spanwise flow is present everywhere above the suction surface and into the wake. The y-z plane in figure 6 adjacent to $S1$ shows that the incoming flow split and traveled partially inboard and partially outboard around the cellular structure of the reversed flow region. In the plane adjacent to the trailing edge, the streamlines wrap into two counter-rotating streamwise rollers on either side of the separated flow. These recirculating regions are no longer present in the next plane downstream, reaffirming that these rollers do not extend far into the wake and diffuse. Rather, they are the same roller, which originates and terminates on the suction surface, and bends into an arch-shape in the near wake.

Figure 6b shows iso-surfaces of helicity. The helicity [34] can be useful to graphically interface with vortical flows [35], and can shed light on the paths of coherent structures [36]. To visualize these behaviours in the shear layers above and beneath the separation bubble, the contours of helicity, colored by normalized spanwise velocity, are presented in figure 6b. Here, the overall helicity $H = \vec{U} \cdot \vec{\omega}$ was used, calculated with the time average of the respective velocity and vorticity vectors. This parameter tracks the relative alignment of the two vectors, and a higher value means that the vorticity and velocity are parallel, meaning higher motion of vortices in the direction of the flow. Of course, to fully grasp the implication of a high helicity contour, one must understand the direction of the respective velocity. As such, the helicity contours are colored by the normalized spanwise velocity component, thus highlighting that vortices on the top shear layer are shedding outboard on the outboard side of the separation bubble and are shedding inboard on the inboard side. Note the lack of high helicity in the center of the separation bubble, which corresponds to the shedding of the most spanwise-oriented portion of the arch vortex, and thus corresponds to the highest perpendicularity between the velocity and vorticity vectors.

C. Unsteady Flowfield

Since at $\alpha = 22°$ the flow was separated over a large portion of the wing, flow unsteadiness associated with vortex shedding must be addressed and is pre-

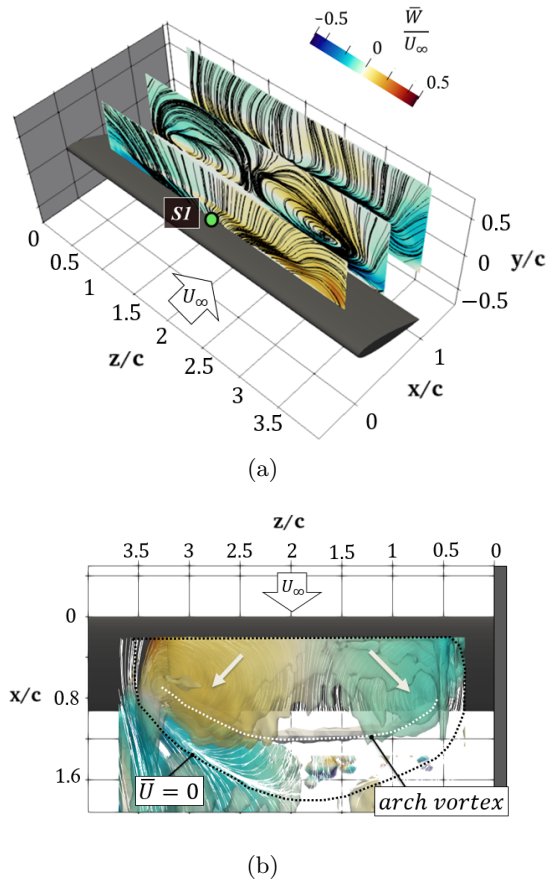

FIG. 6: Spanwise (y-z) planes of color contours of normalized spanwise velocity, $\overline{W}/U_\infty$, superimposed with in-plane streamlines (a), and helicity contours ($\vec{U} \cdot \vec{\omega} = \pm[0.46, 0.6, 0.8]$) colored by normalized spanwise velocity (b). The downstream edge of the separation bubble and the maximum strength of the separation vortex core are marked by the black and white dashed lines, respectively

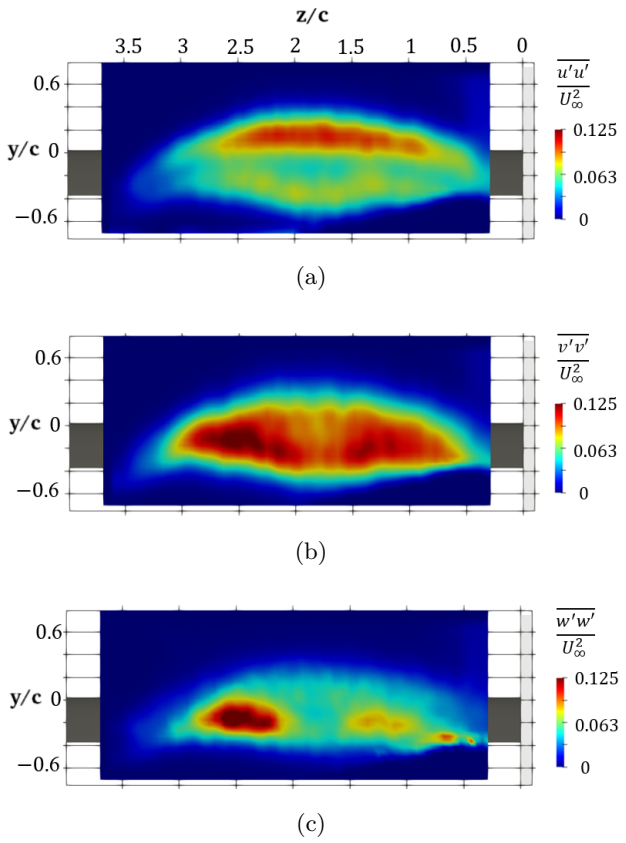

FIG. 7: Color contours of Reynolds stresses at $x/c = 1.75$; $\frac{\overline{u'u'}}{U_\infty^2}$ (a), $\frac{\overline{v'v'}}{U_\infty^2}$ (b), and $\frac{\overline{w'w'}}{U_\infty^2}$ (c). Flow is out of the page.

sented in this section. First, the distributions of the normal Reynolds stresses across the span of the wake at $x/c = 1.75$ are explored in figure 7. For the streamwise Reynolds stress (figure 7a), highest concentration was seen at the midspan above the suction side of the wing, which tapers together on the spanwise limits of the stall cell-shaped separation bubble. The upper and lower shear layers around the stall cell are clearly visualized with the streamwise Reynolds stress. Interestingly, both the vertical and spanwise Reynolds stresses (figures 7b and c, respectively) exhibit the highest magnitudes at the spanwise limits of the stall shape where the upper and lower shear layers taper towards one another. In fact, and in contrast to the wall-to-wall results of [19], $\overline{w'w'}/U_\infty^2$ is of higher magnitude than the other two Reynolds stress components in the flowfield, and the highest concentration of this component occurs along the outboard edge of the stall cell in the wake where the upper and lower shear layers converge. Figure 6b had shown that the helicity concentration that rises under the separation bubble emanating from the outboard surface focus point occurs in the same location as this high magnitude $\overline{w'w'}/U_\infty^2$.

Two more views of the $\overline{w'w'}/U_\infty^2$ concentration are depicted in figure 8 using iso-surfaces. The fact that the helicity and the vertical and spanwise Reynolds stresses have high magnitudes in this region shows that vortices being shed into the wake cause relatively high fluctuations in the vertical and spanwise velocity components, strongly implying that these vortices are nominally streamwise-oriented (at that location). This Reynolds stress distribution is exceedingly similar to those measured in the wake of an artificially induced stall cell on a wall-to-wall model ($AR = 2$) by Manolesos *et al.* [19], however, the magnitudes are different. Whereas Manolesos *et al.* [19] observed the highest magnitude of streamwise Reynolds stress, the present results indicate that the spanwise Reynolds stress is the highest. This can be attributed both to the higher angle of attack and the presence of a tip vortex in the present work. Clearly, the highest concentrations of the turbulent kinetic energy in the flowfield emanates from below and downstream of the stall cell focus point. Analyzing the helicity map sheds

some insight into why this occurs. Figure 6a highlights a structure at the outboard portion of the wing, which shows some similarities to the stall cell vortex identified by simulations of Manolesos *et al.* [19] that originated at the surface focus point. A concentration of helicity below the separation bubble is also colored in blue, arising from the interaction of the trailing edge vortex and the stall cell. This region of high helicity below the separation bubble near the arch vortex corresponds to the highest TKE in the entire flowfield, as shown with the TKE contours in figure 6c.

Next, the link between the Reynolds stress cross-product $\overline{u'w'}/U_\infty^2$ and the helicity at the outboard portion of the model is shown in figure 9, where figure 9a presents the helicity contours and figure 9b shows the contours of the streamwise-spanwise cross Reynolds stress. Near surface streamlines (white) and 3D streamlines marking the center location of the arch vortex (black) are shown for reference. There is an overlap of two of the flow structures identified with each of the respective contours. The streamwise-oriented structure is seen to form outboard of the surface focus in both subfigures, implying that this is a secondary structure created from interaction between the attached flow near the tip and the reversed flow in the midspan separation region. Note that this view shows that the streamwise-oriented structure is **not** emanating from the stall cell focus itself, but rather from outboard and slightly above the surface focus. This finding is in contrast to that of Manolesos *et al.* [19] and this is likely because the type of separation measured here is not a closed stall cell but rather a full wing stall, though it is noteworthy that a similar vortical structure is present. Moreover, the model used by Manolesos *et al.* [19] is wall-to-wall, whereas in the present work the model is cantilevered, which is associated with a tip vortex that is absent in Manolesos *et al.* [19] work. The presence of the tip vortex increases the downwash onto the spanwise region including the outboard surface focus, thus strengthening the secondary streamwise-oriented structure identified in the helicity. Another notable similarity to the helicity and $\overline{u'w'}/U_\infty^2$ contours is that a concentration appears at the same location as the high-magnitude $\overline{w'w'}/U_\infty^2$ and TKE identified in figure 8.

To further explore the correlations between the streamwise/vertical Reynolds stresses and the vertical/spanwise Reynolds stresses, three-dimensional isosurfaces of $\overline{u'v'}/U_\infty^2$ and $\overline{v'w'}/U_\infty^2$ are presented in figure 10. The blue (negative) contour of $\overline{u'v'}/U_\infty^2$ in figure 10a is directly downstream of the arch vortex, while the orange (positive) contour is below the blue contour and downstream of the trailing edge of the model. It can be seen that the highest magnitude of $\overline{u'v'}/U_\infty^2$ is at the downstream edge of the separation bubble, showing that this is the region of highest momentum transfer across the upper and lower shear layers associated with shedding of spanwise vorticity into the wake.

Elyasi and Ghaemi [37] conducted an experimental investigation of a turbulent separation due to an adverse pressure gradient, and showed that peaks of $\overline{u'v'}$ were in regions of correlated fluctuations of streamwise and vertical velocity due to the roll-up of out-of-plane (spanwise) vortical structures. The present results complement this finding: the peaks of negative and positive $\overline{u'v'}$ correspond to the regions of the leading edge and trailing edge shear layers, respectively.

At the spanwise limits of these concentrations of $\overline{u'v'}/U_\infty^2$ $(1 < z/c < 3))$ high magnitude concentrations of $\overline{v'w'}/U_\infty^2$ are seen in figure 10b. Near the outboard surface focus, a high magnitude of negative $\overline{v'w'}/U_\infty^2$ extends into the wake at a similar orientation to the high $\overline{w'w'}/U_\infty^2$ (figure 8) while a positive contour mirrors it emanating from the inboard surface focus. These contours are at the same vertical location as the arch vortex and the positive $\overline{u'v'}/U_\infty^2$ contours as they lie above the downstream limit of the separation bubble. Below these contours at the vertical location of the trailing edge (below the downstream limit of the separation bubble), smaller regions of positive and negative $\overline{v'w'}/U_\infty^2$ are present, which have the opposite sign of the above regions. This same pattern was seen in the wake of the artificially induced stall cell in the results of Manolesos *et al.* [19], who reasoned these high $\overline{v'w'}/U_\infty^2$ regions were regions of vortex stretching and deformation. The present analysis implies that the arch vortex is similarly deformed as it is shed into the wake. One striking difference between the present results and [19] is the large positive contour of $\overline{v'w'}/U_\infty^2$ near the wing's tip, reminiscent of a streamwise-oriented roller that originated on the suction surface outboard of the outboard surface focus and extended into the wake. This is most likely as a direct result of the free end and associated interactions between the tip vortex and the midspan stall cell flow structure.

To further explore the unsteady behaviour of the separated flow over the $sAR = 4$ wing, two spanwise locations were selected for temporal analysis using TR-SPIV. The first spanwise location is at the saddle point S1, the stall cell stagnation point identified from the OFV and the SPIV. At this location, the separation is expected to resemble a typical 2-D separation. The second location is at the focus F1. It was chosen to give a view of the unsteady behavior at the outboard focus point of the stall cell structure.

The characteristic frequencies present in the flow were obtained by performing a spectral analysis on the vertical velocity component from the TR-SPIV data. In order to visualize the spectral content in the wake, power spectral density (PSD) contours were calculated. The PSD was calculated using Welch's method (Matlab function pwelch) with window size $N/10$, and overlapping windows at 95% the window size. This calculation was performed across the time history of the vertical velocity within select TR-SPIV interrogation windows $v(i, j)$ where i is a single selected x/c location and j is the range of y/c stations in the PIV plane corresponding to i. Figure 11 presents two x/c locations for the stall cell center

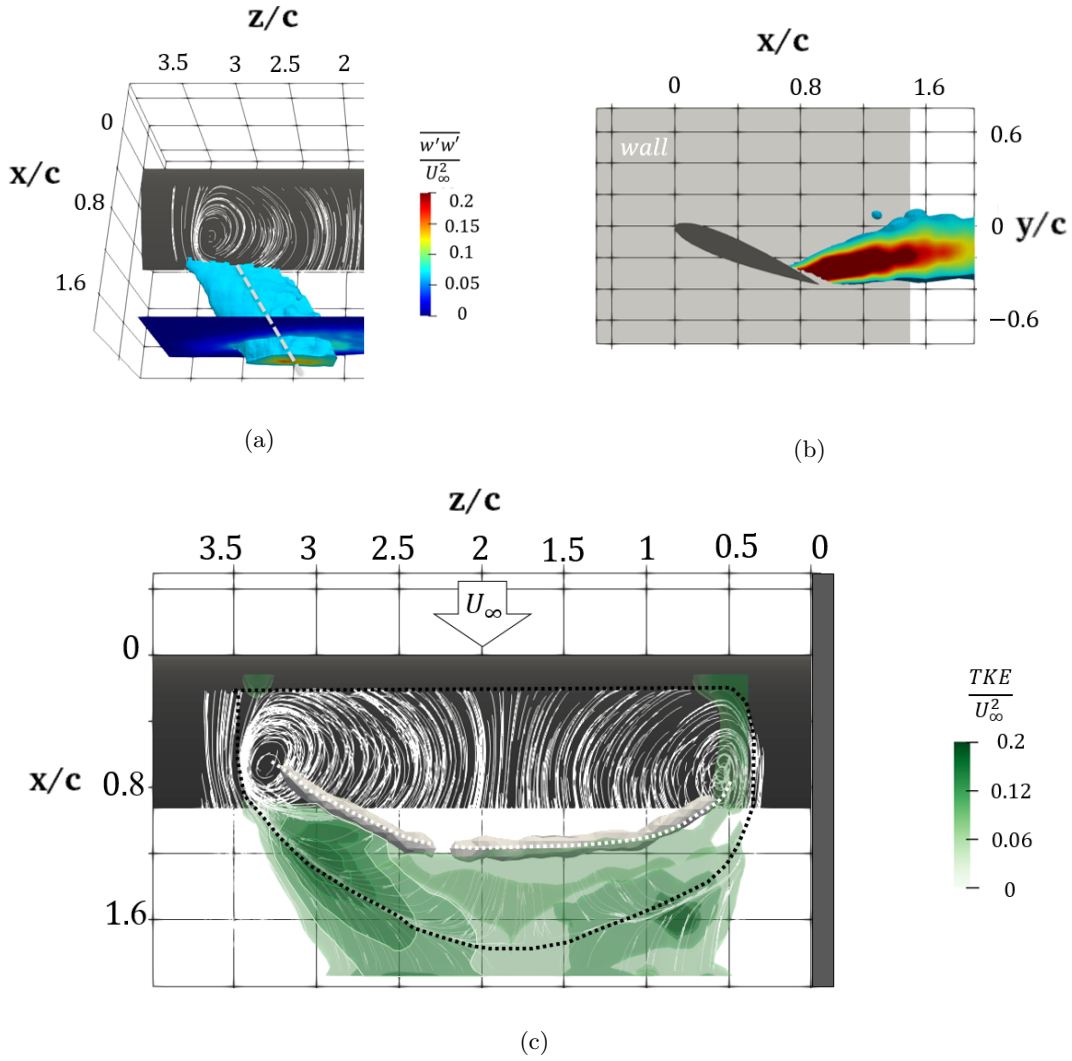

FIG. 8: Iso-volume of $\overline{w'w'}/U_\infty^2 > 0.06$ superimposed with near-surface streamlines and the color contours of $\overline{w'w'}/U_\infty^2$ at $x/c = 1.75$ (a), and a z-normal view of the same iso-volume, bisected along its core (b), and 3D color contours of the normalized TKE (c). The downstream edge of the separation bubble and the maximum strength of the separation vortex core are marked by the black and white dashed lines, respectively.

($z/c = 1.75$). The x/c locations are shown on the left of figures 11a and c with a vertical line marker superimposed over the mean $\overline{U}$ contours. The power multiplied by the differential frequency df is shown in blue contours on the right of each sub-figure (figures 11b and d, respectively), and the frequencies are represented with Strouhal number, where: $St = \frac{fcsin(\alpha)}{U_\infty}$. The PSD in the wake along the stall cell center shows a definite dominance of the shedding frequency ($St = 0.17$) across the entire wake;

Unlike the spectral content along the stall cell center ($z/c = 1.75$), the trend of the spectral content along the focus center location ($z/c = 3.3$) is not as clear. Shown in figure 12 are the power contours at two streamwise locations in the wake along the focus center at $x/c = 1.05$ and $x/c = 1.25$. At these locations, the spectral content is spread over multiple frequencies. At the upstream location (figure 12a), the frequencies with the highest power are located at the y/c locations of the shear layers on either side of the wake. Farther downstream (at $x/c = 1.25$, figure 12b), the power begins to shift towards the wake's shedding frequency. However, even at this location it is still hard to discern a dominant frequency, showing that the unsteady flowfield in the wake along the focus center of the stall cell is clearly less coherent than that along the stall cell center. Still, the highest peaks occur near the shedding frequency at $St = 0.19$ and $St = 0.21$. A line plot of the spectra at $y/c = -0.3$ comparing the peaks of these frequencies (not shown for brevity) showed that the amplitudes at both St numbers were very similar.

The frequency increase at the focus center can be ex-

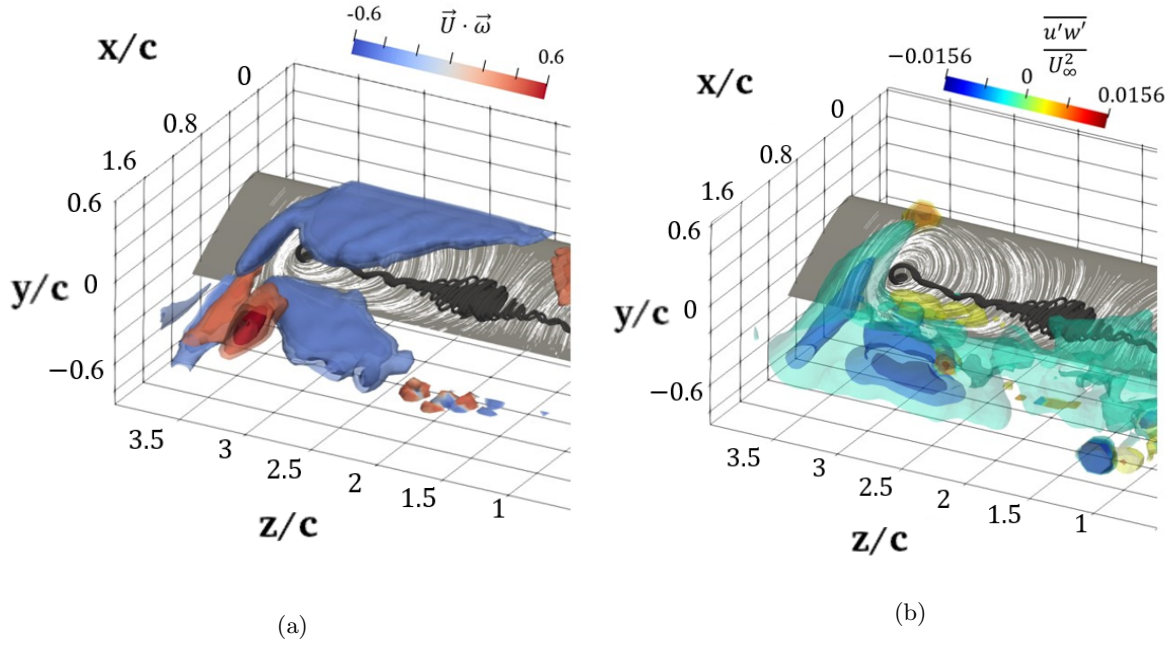

(a) (b)

FIG. 9: 3-D helicity contour (a), and 3-D contour of streamwise-spanwise cross Reynolds stress $\overline{u'w'}/U_\infty^2$ (b). Both sub-figures are superimposed with near-surface streamlines (white) and 3-D streamlines marking the center location of the arch vortex (black). Flow is from top right to bottom left.

plained by the decrease in the size of the recirculation bubble at this spanwise station compared to the stall cell center location. As the separation bubble size decreases, the displacement thickness decreases, and since displacement thickness varies inversely with frequency, the frequency in the PSD estimate increases. Also, it was seen in several studies at lower Reynolds numbers ([38],[39]) that vortex dislocations would occur at the spanwise limits of a shedding cell on unswept wings with $sAR \gtrapprox 4$. These dislocations resulted in two peaks in the PSD, one corresponding to the shedding frequency and one corresponding to an interaction mode. It is hypothesized that a similar mechanism is present in the present results, but investigations of the frequency content at more spanwise locations is required to draw this conclusion definitively, which is a topic for future work.

The band of frequencies with elevated power at this spanwise location of the stall cell focus point is notably different from the single peak of the shedding frequency seen in the PSD at stall cell center. A plausible explanation for this stems from the existence of two dominant spectral peaks at this location for the frequencies $St = 0.19$ and $St = 0.21$. The interplay between this two similar but disparate frequencies in the flowfield could result in beating, leading to power allocation towards frequencies equal to the sum or difference of the two dominant frequencies. Non-linear interactions between the beating frequencies and the original frequencies would lead to this band of amplified frequencies in the flow.

Now that the characteristic frequencies of wake shedding have been identified, coherent structures corresponding to the shedding frequency is visualized in the plane across the center of the stall cell. The instantaneous vertical velocity component at the stall cell center is shown in figures 13 and 14 as color contours as a function of time normalized by the period time of the shedding frequency, t/T, and vertical position y/c. Figure 13 is at $x/c = 1.05$ and figure 14 is at $x/c = 1.25$. Contrasting the two streamwise locations reveals that the magnitude and coherence of the fluctuations in the vertical velocity component increases moving downstream into the wake. For example, there are low-magnitude fluctuations visible from $t/T = 55$ to 65 at $x/c = 1.05$ in figure 13. These same fluctuations are present in figure 14 at $x/c = 1.25$, though the magnitude is notable increased. This is a similar result shown in figure 11 as the power of the shedding frequency in the PSD estimate increased significantly moving from $x/c = 1.05$ to $x/c = 1.25$.

The instantaneous results reveal the wake shedding was an intermittent phenomenon. Even though these results were measured at the center of the stall cell and expected to exhibit quasi-2D shedding, the periodicity of the shedding was not constant. This intermittence is shown quite plainly in figure 14. High-magnitude fluctuations of v/U_∞ show up in disparate packets over time, with highest peaks occurring at $t/T = 30\pm5$, 60 ± 10, and 132 ± 12. Between the regions of the higher-magnitude shedding, the time-history of vertical velocity still show some semblance of the shedding pattern, but the fluctuations are far less consistent and with lower magnitude. In

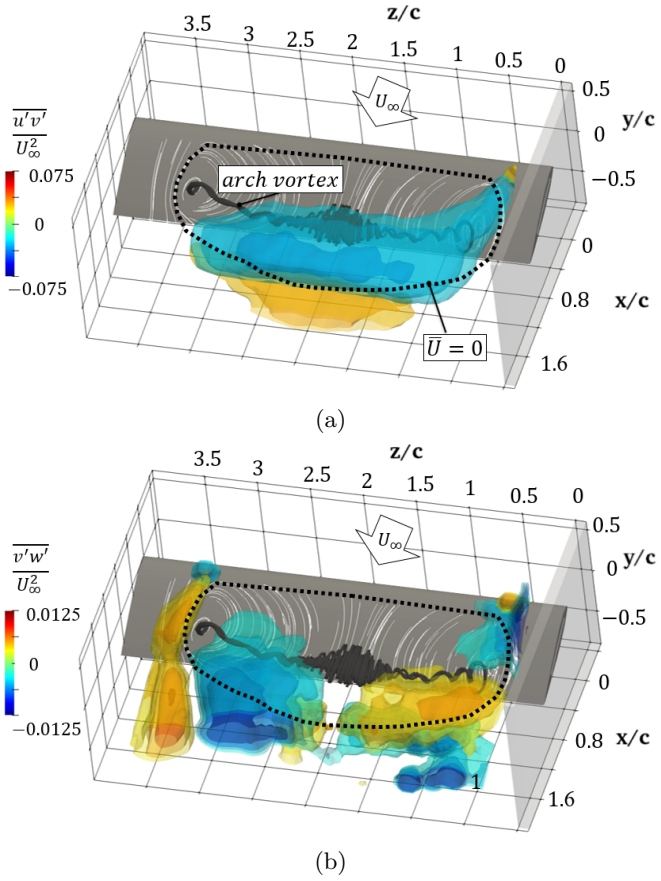

FIG. 10: Iso-volumes of cross-stream Reynolds stresses; $\frac{\overline{u'v'}}{U_\infty^2}$ (a), and $\frac{\overline{v'w'}}{U_\infty^2}$ (b). Near-surface streamlines (white), arch vortex streamlines (black), and the outline of the separation bubble (dashed line) are included.

addition, a band of characteristic frequencies are present as the coherence of the shedding is diminished.

The impact of the intermittence of the shedding on the frequency content in the flowfield is examined more closely in figure 15 with a spectrogram of the vertical velocity at $(x/c, y/c) = 1.25, -0.2)$ from $t/T = 48$ to 94. Note that the spectrogram was calculated from the same vertical velocity signal displayed in the second row of figure 14. The power associated with the shedding frequency ($St = 0.17$) has high amplitude from $t/T = 50$ to 70 and decreases sharply for $t/T > 70$ as the shedding is disrupted. This turning on and off of the shedding phenomenon results in a low-frequency oscillation of the velocity components on the order of 10% the shedding frequency. This low frequency was seen in the PSD estimates at both the stall cell center and the stall cell focus point center spanwise locations. At both locations, this low frequency mode has highest power at the vertical locations corresponding to reverse flow. This is compelling evidence for a periodic movement of the cell on the surface of the wing, and as the cell moves, the power of the shedding frequency is augmented intermittently. A similar low frequency oscillation of the stall cell has been reported by Zaman and Mckinzie [13].

A single shedding cycle with high magnitude fluctuations is examined in figure 16 with color contours of instantaneous vertical velocity. For all the sub-figures the in-plane velocity vectors are superimposed. Vortices in each frame are identified with the peaks of Γ_1 are shown as scattered points, colored green if the rotation is counter-clockwise (positive spanwise vorticity) or red if the rotation is clockwise (negative spanwise vorticity). For the first half of the cycle, a region of upwash rises from the bottom of the frame and is balanced by a downwash from the top of the frame in the second half of the cycle. This behaviour is correlated to the shedding and passage into the wake of a counter-clockwise vortex initiating at the trailing edge. The path of this trailing edge vortex is tracked with the green scatter dot in figure 16. From the leading edge and riding along the upper shear layer of the separation ($y/c \approx 0$) a vortex (marked with the red dot) travels into the wake and counter-rotates the trailing edge vortex.

To investigate the behavior of coherent structures on average over a series of ten shedding cycles ($t/T = 55$ to $t/T = 65$ from figure 14), the velocity components obtained from the TR-SPIV were phase-averaged about the shedding frequency, as shown in figure 17. The top row shows the streamwise component, the second row the vertical component, and the bottom row the spanwise component of phase-averaged velocity. The streamwise and vertical velocity components clearly showed the advection of a counter-clockwise-rotating vortex across the interrogation window in figures 17a-c. The green point of Γ_1 consistently tracked the vortex along its path, which exactly coincides with trailing edge shear layer and the lower boundary of the separation bubble. The rollup of this vortex was accompanied by a high-magnitude upwash at $t/T = 0.167$ (figure 17a), and as it advects across the frame, a corresponding downwash at $t/T = 0.5 - 0.667$ (figures 17c-d). As the high magnitude downwash advects across the frame and the next upwash of the following trailing edge vortex rollup begins, these average-subtracted velocity components exhibit a counter-rotating swirl that follows the path of the first vortex. The Γ_1 also identified this as a vortex with clockwise rotation. This is an interesting result, as only the trailing edge vortex (with its counter-clockwise rotation in this reference frame) is expected to advect into the wake along the trailing edge shear layer. However, as shown by visualizations of the vortex shedding phenomenon measured by Yarusevych *et al.* [40], for the most part the large-scale vortices shed from the leading and trailing edges would roll-up at approximately the same (x,y) station. This means that the vortices shed from the leading edge are drawn downwards by the downwash of the wake and as a result follow a similar path to that of the trailing-edge vortices. [floatfix]

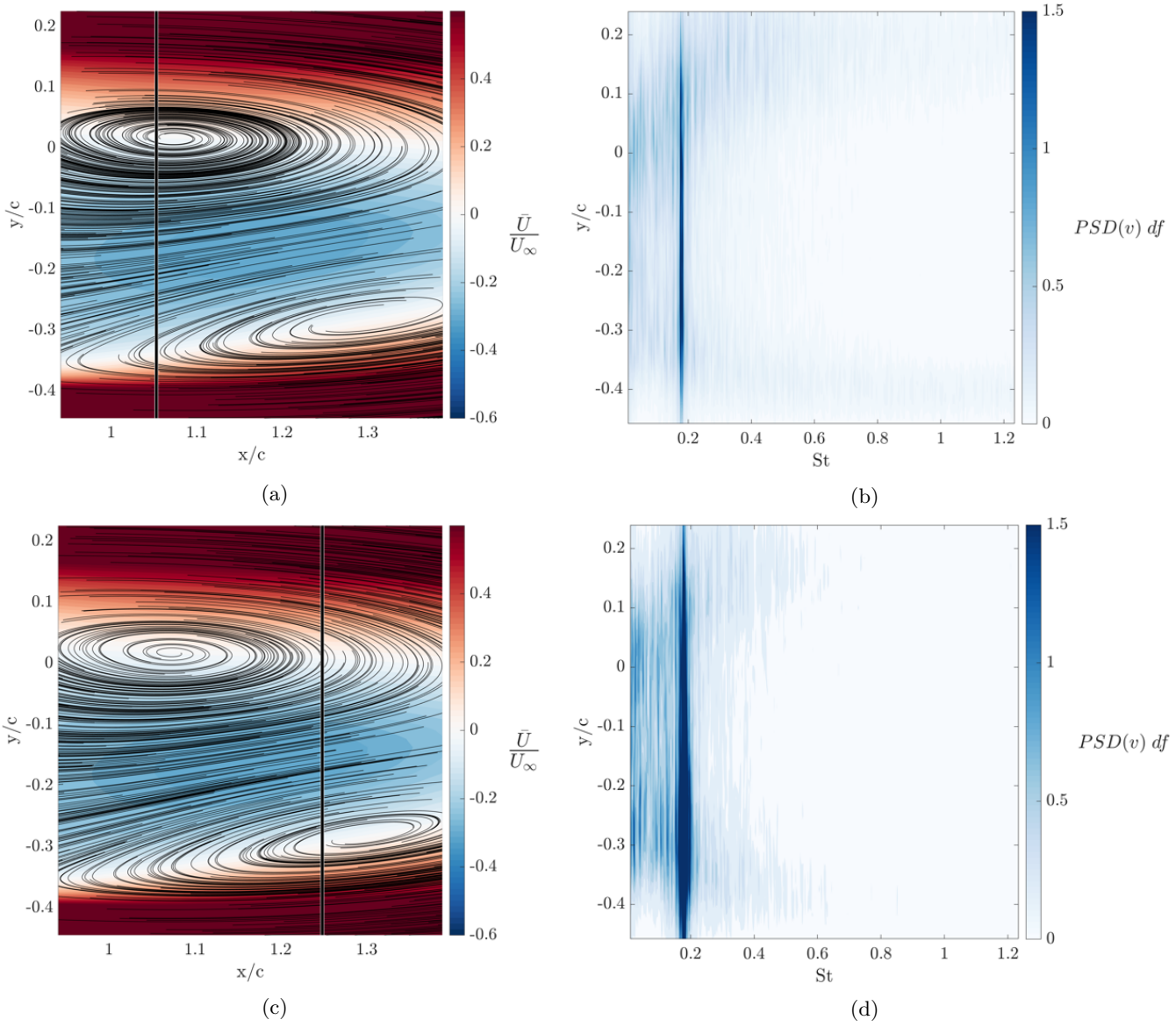

FIG. 11: Color contours of time-averaged normalized streamwise velocity (a, c), and the vertical variance of power spectra (b, d) for the vertical velocity component at $x/c = 1.05$ (a, b) and $x/c = 1.25$ (c, d) in the near wake along the stall cell center location. Flow is from left to right.

IV. CONCLUSIONS

An experimental investigation was performed on cantilevered, unswept wings with constant cross section of NACA 0015 and semi-aspect ratios of $sAR = 1, 2, 4$. Data were collected at Reynolds number $Re_c = 3.3 \times 10^5$. Oil flow visualizations characterized the surface topology at angles of attack between 15° and 22°. Quantitative flowfield measurements using TR-SPIV and SPIV at an angle of attack of 22° characterized the fluctuating and mean flowfields for the wing in deep stall.

The OFV results showed that for $sAR = 1$, 2, and 4 two counter-rotating surface foci developed on the suction surface on the borders of the mid-span reverse flow. As aspect ratio was decreased, the angle of attack at which flow separation was present was increased. In all cases, separation was accompanied by two counter-rotating foci which form on the suction surface. For semi-aspect ratios, $sAR = 1$, 2, and 4, the outboard and inboard surface foci are formed due to interactions of the midspan separation with the tip vortex and horseshoe vortex, respectively. The foci were shown to be the direct result of end effects. At lower semi-aspect ratios the tip and root encourage flow reattachment, thus delaying separation until a higher angle of attack than the large aspect ratio case. As expected for the range of aspect ratios studied, only one separation (stall) cell was seen for each case.

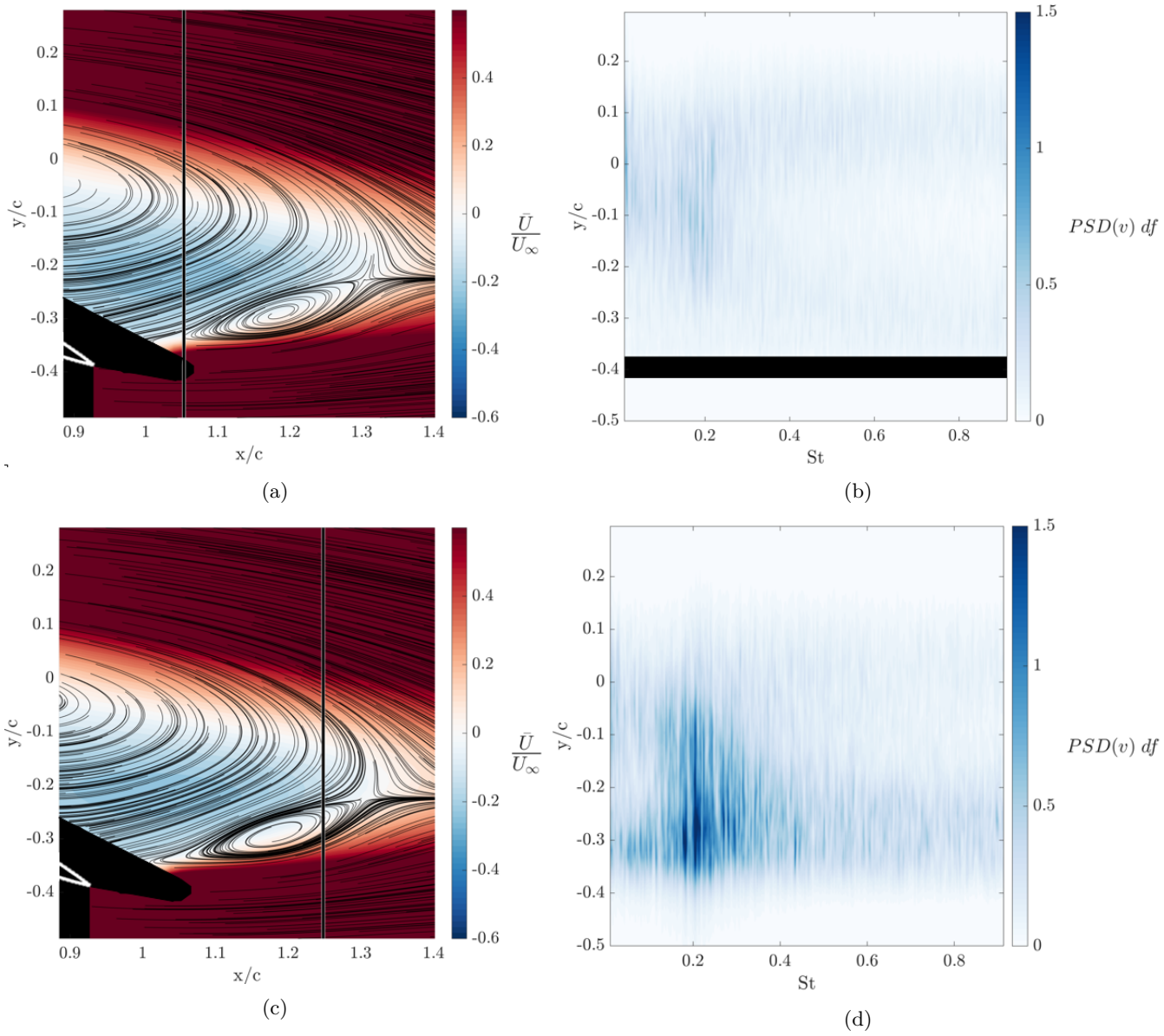

FIG. 12: Color contours of time-averaged normalized streamwise velocity (a, c), and the vertical variance of power spectra (b, d) for the vertical velocity component at $x/c = 1.05$ (b) and $x/c = 1.25$ (d) in the near wake along the focus center location. Flow is from left to right.

The time-averaged volumetric flowfield of the $(sAR, \alpha) = (4, 22°)$ configuration was investigated with SPIV. The flowfield structure was characterized by an arch vortex which terminated on either of the surface foci identified with the OFV. A survey of the 3-D streamlines, x-y planar streamlines, Γ_1, MHM, and $vflow$ vortex identification techniques revealed good agreement on the location of the arch vortex. The Reynolds stresses associated with the separated shear layers revealed that the upper shear layer above the arch vortex was associated with high magnitudes in $\overline{u'u'}$ and $\overline{v'v'}$, which is related to increased transfer of momentum across this layer. The spanwise Reynolds stress, $\overline{w'w'}$, had the highest magnitude downstream of the surface foci and under the reversed flow region that extended into the wake. This spanwise Reynolds stress was found to be the highest contributor to the overall flowfield TKE. The Reynolds shear stresses were compared to previous results of an induced stall cell over a wall-to-wall model. Some similarities were seen: the $\overline{u'v'}/U_\infty^2$ has the highest magnitude and the $\overline{u'w'}/U_\infty^2$ has the lowest magnitude of the Reynolds shear stresses, and the location of these stresses' peaks correspond to momentum transfer across shear layers. The $\overline{v'w'}/U_\infty^2$ peaks were seen to have a similar structure at the downstream limit of the separation bubble, however, in

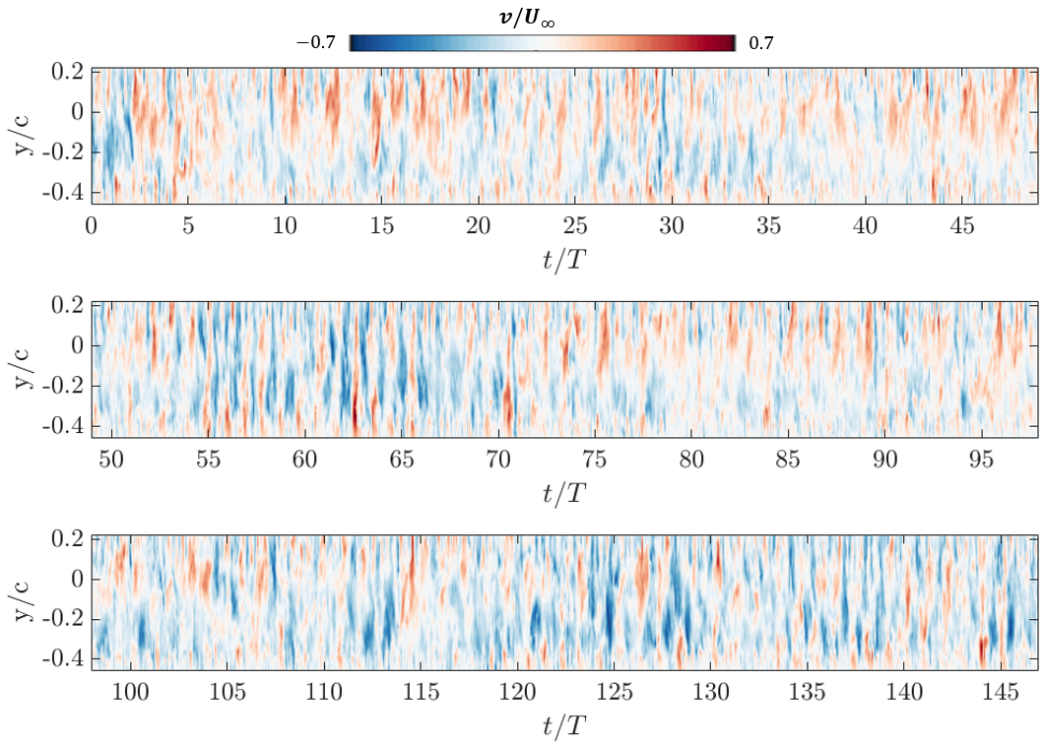

FIG. 13: Color contours of normalized instantaneous vertical velocity at $x/c = 1.05$ at the stall cell center location. Time is normalized by the period of the shedding frequency, T.

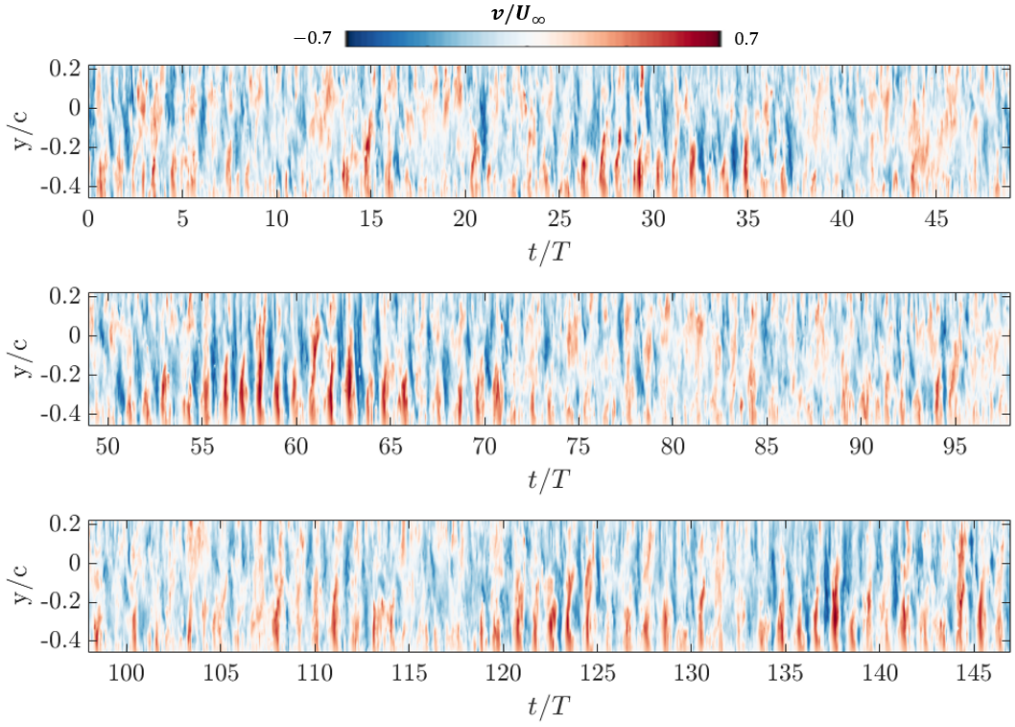

FIG. 14: Color contours of normalized instantaneous vertical velocity at $x/c = 1.25$. Time is normalized by the period of the shedding frequency, T.

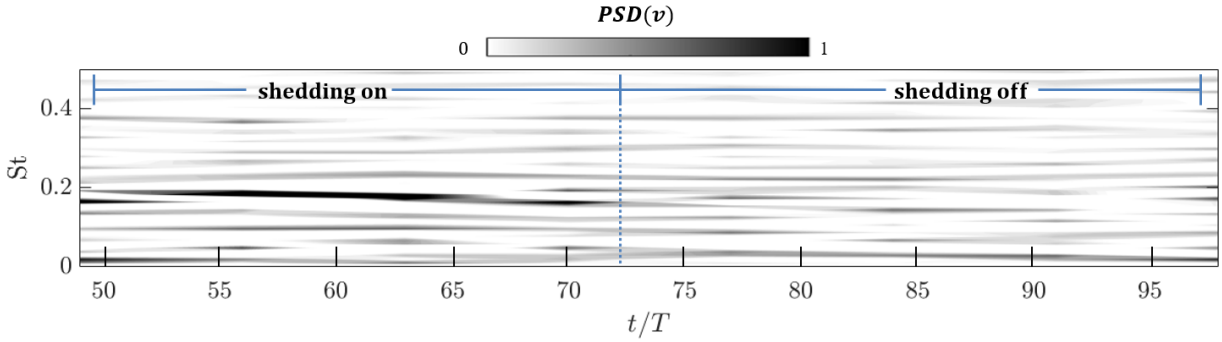

FIG. 15: Spectrogram of vertical velocity component corresponding to the second row of figure 14 at $(x/c, y/c) = (1.25, -0.2)$.

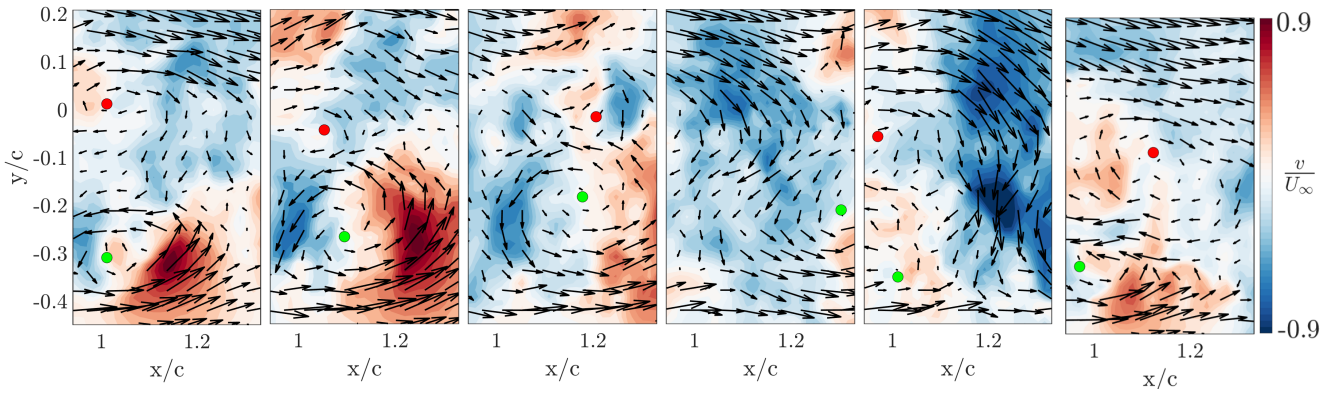

(a) t/T = 56.15 (b) t/T = 56.3 (c) t/T = 56.43 (d) t/T = 56.57 (e) t/T = 56.78 (f) t/T = 56.85

FIG. 16: Color contours of instantaneous vertical velocity v/U_∞ for a single shedding cycle (see figure 14 for corresponding times) at the stall cell center location with in-plane velocity vectors superimposed. Vortex cores are identified with Γ_1 peaks, where a red dot denotes clockwise rotation and a green dot denotes counter-clockwise rotation. Flow is from left to right.

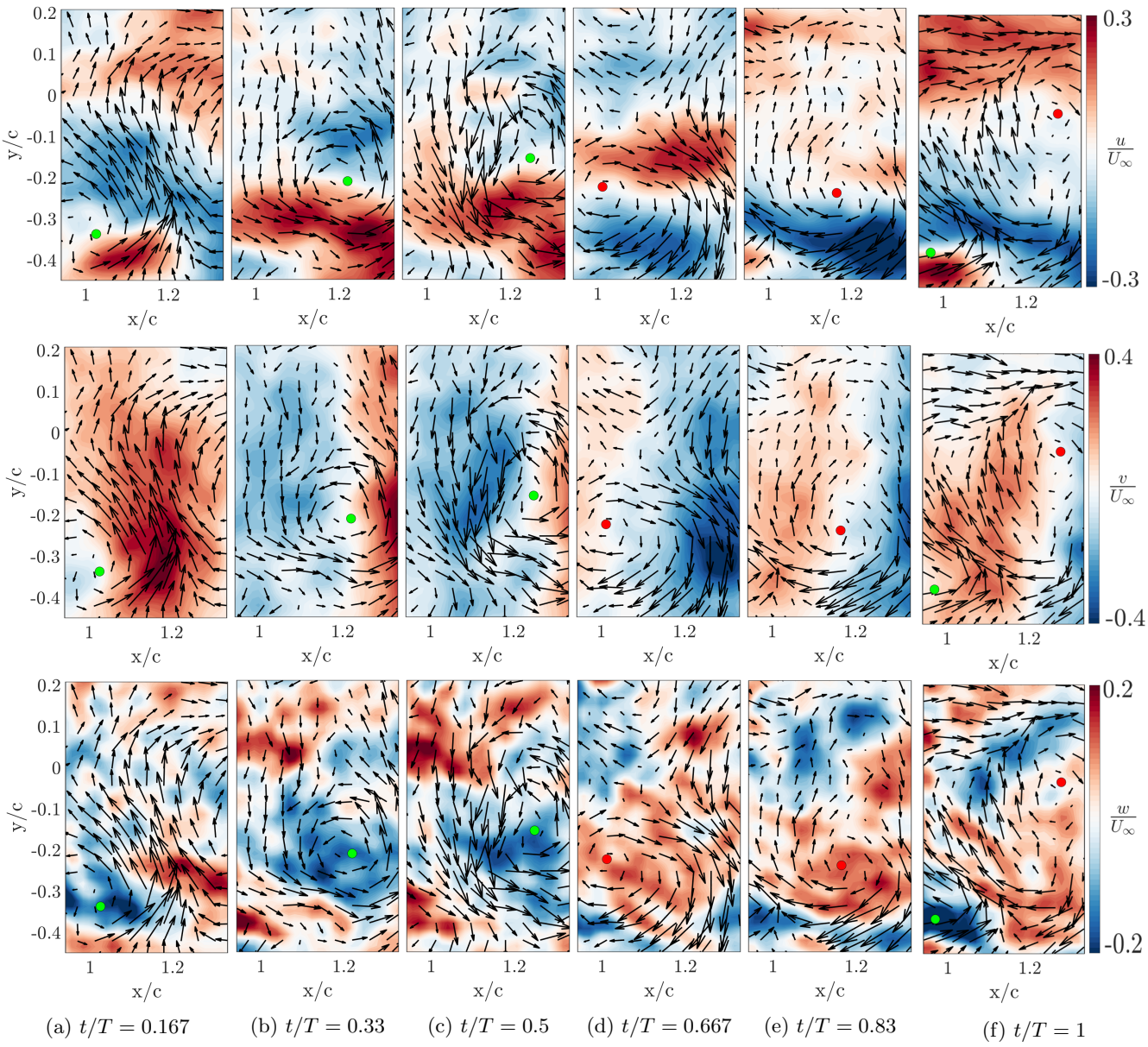

FIG. 17: Color contours of phase-averaged mean-subtracted u/U_∞ (first row) v/U_∞ (second row) w/U_∞ (third row) at the stall cell center location with in-plane velocity vectors superimposed. Vortex cores are identified with Γ_1 peaks, where a red dot denotes clockwise rotation and a green dot denotes counter-clockwise rotation. Flow is from left to right.

the present case the presence of the tip vortex causes the formation of a new $\overline{u'v'}/U_\infty^2$ concentration located between the tip vortex and the separation region.

The characteristic frequencies in the flowfield were explored using TR-SPIV. At the midspan, the shedding frequency was identified to be $St = 0.17$. Directly downstream of the trailing edge at the midspan, phase-averaged images of the shedding cycle showed that the shedding of both the trailing edge vortex and the separation arch vortex directly followed the path of the reversed flow region, rising vertically from the trailing edge to the mid-wake. Analysis of the instantaneous vertical velocity field showed a similar result while highlighting how intermittent the shedding phenomenon was. A spectrogram of the vertical velocity fluctuations clearly showed the power of the shedding frequency increased and decreased over time, which is evidence of the movement of the stall cell over time.

The wake downstream of the focus point was highly influenced by the three-dimensionality of the flowfield. Two frequencies $St = 0.19$ and $St = 0.21$ were present at the focus center PSD and these could be evidence of vortex dislocation [38][39]. The Reynolds stresses associated with correlated fluctuations of spanwise velocity had

the largest amplitude downstream of the focus points, whereas the helicity was lowest downstream of the stall cell center, as the shedding of nominally spanwise vortices made $\vec{U}$ and $\vec{\omega}$ orthogonal, and the flowfield was the least three-dimensional at this location.

ACKNOWLEDGMENTS

This work was supported by the Air Force Office of Scientific Research grant number: FA9550-17-1-0222.

[1] A. E. Winkelman and J. B. Barlow, Flowfield Model for a Rectangular Planform Wing beyond Stall, AIAA Journal **18**, 1006 (1980).

[2] A. V. Boiko, A. V. Dovgal, B. Y. Zanin, and V. V. Kozlov, Three-dimensional structure of separated flows on wings (review), Thermophysics and Aeromechanics **3**, 1 (1996).

[3] F. Plante, J. Dandois, S. Beneddine, É. Laurendeau, and D. Sipp, Link between subsonic stall and transonic buffet on swept and unswept wings: From global stability analysis to nonlinear dynamics, Journal of Fluid Mechanics **908**, 10.1017/jfm.2020.848 (2020).

[4] S. A. Yon and J. Katz, Study of the unsteady flow features on a stalled wing, AIAA Journal **36**, 305 (1998).

[5] A. P. Broeren and M. B. Bragg, Spanwise variation in the unsteady stalling flowfields of two-dimensional airfoil models, AIAA Journal **39**, 2001 (2001).

[6] G. McCullough and D. Gault, *Examples of three representative types of airfoil-section stall at low speed*, Tech. Rep. (Ames Aeronautical Laboratory, Moffett Field, CA, 1951).

[7] D. Weihs and J. Katz, Cellular patterns in poststall flow over unswept wings, AIAA Journal **21**, 1757 (1983).

[8] A. Gross, H. F. Fasel, and M. Gaster, Criterion for spanwise spacing of stall cells, AIAA Journal **53**, 272 (2015).

[9] S. C. Crow, Stability theory for a pair of trailing vortices, AIAA Journal **8**, 2172 (1970).

[10] D. Rodríguez and V. Theofilis, On the birth of stall cells on airfoils, Theoretical and Computational Fluid Dynamics **25**, 105 (2011).

[11] W. He, R. S. Gioria, J. M. Pérez, and V. Theofilis, Linear instability of low Reynolds number massively separated flow around three NACA airfoils, Journal of Fluid Mechanics **811**, 701 (2017).

[12] H. Dell'Orso, B. A. Tuna, and M. Amitay, Measurement of Three-Dimensional Stall Cells on a Two-Dimensional NACA0015 Airfoil, AIAA Journal **54**, 3872 (2016).

[13] K. Zaman and D. Mckinzie, *A natural low frequency oscillation in the wake of an airfoil near stalling conditions*, Tech. Rep. February 1988 (NASA, Cleveland, Ohio, 1988).

[14] J. Liu and Z. Xiao, Low-Frequency Oscillation over NACA0015 Airfoil Near Stall at High Reynolds Number, AIAA Journal **58**, 1 (2019).

[15] J. M. Délery, Robert Legendre and Henri Werlé: Toward the Elucidation of Three-Dimensional Separation, Annual Review of Fluid Mechanics **33**, 129 (2001).

[16] M. Tobak and D. J. Peake, Topology of three-dimensional separated flows, Annual Review of Fluid Mechanics **14**, 61 (1982).

[17] R. L. Maltby, Flow visualization in wind tunnels using indicators (1962).

[18] A. Ma, B. Gibeau, and S. Ghaemi, Time-resolved topology of turbulent boundary layer separation over the trailing edge of an airfoil, Journal of Fluid Mechanics 10.1017/jfm.2020.106 (2020).

[19] M. Manolesos, G. Papadakis, and S. Voutsinas, An experimental and numerical investigation on the formation of stall-cells on airfoils, Journal of Physics: Conference Series **555**, 012068 (2014).

[20] E. P. DeMauro, H. Dell'Orso, V. Sivaneri, B. A. Tuna, and M. Amitay, Measurements of 3-D stall cells on 2-D airfoils, in *45th AIAA Fluid Dynamics Conference* (American Institute of Aeronautics and Astronautics Inc, AIAA, 2015).

[21] H. Dell'Orso and M. Amitay, Parametric investigation of stall cell formation on a NACA 0015 airfoil, AIAA Journal **56**, 3216 (2018).

[22] A. Sciacchitano and B. Wieneke, PIV uncertainty propagation, Measurement Science and Technology **27**, 10.1088/0957-0233/27/8/084006 (2016).

[23] L. Benedict and R. Gould, Towards better uncertainty estimates for turbulence statistics, Experiments in Fluids **22**, 10.1007/s003480050030 (1996).

[24] S. C. Yen and L. C. Huang, Flow patterns and aerodynamic performance of unswept and swept-back wings, Journal of Fluids Engineering, Transactions of the ASME **131**, 1111011 (2009).

[25] C. E. Toppings and S. Yarusevych, Structure and dynamics of a laminar separation bubble near a wingtip, Journal of Fluid Mechanics **929**, 1 (2021).

[26] L. Dong, K. S. Choi, and X. Mao, Interplay of the leading-edge vortex and the tip vortex of a low-aspect-ratio thin wing, Experiments in Fluids **61**, 1 (2020).

[27] A. E. Winkelmann, The effects of aspect ratio on the stall of a finite wing, in *27th AIAA Aerospace Sciences Meeting* (1989).

[28] V. Y. Neiland and G. Stolyarov, On one type of separated flow on a rectangular wing, Uch. Zap. TsAGI **13**, 83 (1982).

[29] T. Carvajal, T. Guha, and M. Amitay, Flowfield over a generic tailless chined forebody-delta wing configuration (2022).

[30] V. Holmén, *Methods for Vortex Identification*, Master of science, Lund University (2012).

[31] J. Jeong and F. Hussain, On the identification of a vortex, Journal of Fluid Mechanics **285**, 69 (1995).

[32] L. Graftieaux, M. Michard, and N. Grosjean, Combining PIV, POD and vortex identification algorithms for the study of unsteady turbulent swirling flows, Measurement Science and Technology **12**, 1422 (2001).

[33] R. L. Simpson, On turbulent boundary-layer separation, Annual Review of Fluid Mechanics **21**, 205 (1989).

[34] H. Moffatt and A. Tsinober, Helicity in laminar and turbulent flow, Annual Review of Fluid Mechanics **24**, 281 (1992).

[35] Y. Levy, D. Degani, and A. Seginer, Graphical visualization of vortical flows by means of helicity, AIAA Journal **28**, 1347 (1990).

[36] F. Hussain, Coherent Structure and turbulence, Journal of Fluid Mechanics **173**, 303 (1986).

[37] M. Elyasi and S. Ghaemi, Experimental investigation of coherent structures of a three-dimensional separated turbulent boundary layer, Journal of Fluid Mechanics **859**, 1 (2019).

[38] K. Zhang, S. Hayostek, M. Amitay, W. He, V. Theofilis, and K. Taira, On the formation of three-dimensional separated flows over wings under tip effects, Journal of Fluid Mechanics 10.1017/jfm.2020.248 (2020).

[39] A. Burtsev, W. He, K. Zhang, V. Theofilis, K. Taira, and M. Amitay, Linear modal instabilities around post-stall swept finite wings at low Reynolds numbers, Journal of Fluid Mechanics **944**, 1 (2022).

[40] S. Yarusevych, P. E. Sullivan, and J. G. Kawall, On vortex shedding from an airfoil in low-Reynolds-number flows, Journal of Fluid Mechanics **632**, 245 (2009).